Interpenetrating Gyroid Lattice - Foam Composites with Synergistically Enhanced Stiffness and Energy Absorption for Impact Mitigation

Jizhe Cai[a,b,c,d,*], Bhanugoban Maheswaran[d], Emmanuel Dada[a], Hridyesh Tewani[e], Pavana Prabhakar[d,e], Ramathasan Thevamaran[d, *]

[a] Department of Industrial & Manufacturing Engineering, Florida A&M University-Florida State University College of Engineering, Tallahassee, FL 32310
[b] Department of Mechanical & Aerospace Engineering, Florida A&M University-Florida State University College of Engineering, Tallahassee, FL 32310
[c] High-Performance Materials Institute, 2005 Levy Ave., Tallahassee, FL, 32310
[d] Department of Mechanical Engineering, University of Wisconsin-Madison, Madison, WI 53706.
[e] Department of Civil and Environmental Engineering, University of Wisconsin-Madison, Madison, WI 53706
[*]Corresponding author emails: jcai@eng.famu.fsu.edu (JC); thevamaran@wisc.edu (RT)

Abstract

Advanced lightweight structural materials require both high stiffness and energy-absorption capacity for demanding protective applications. Low-density polymer foams offer excellent specific energy absorption but have inadequate stiffness and structural stability for load-bearing applications. Stiff structural materials, on the other hand, provide load-bearing capacity at the expense of deformability and energy absorption capacity. Here, we overcome this trade-off by creating lattice–foam interpenetrating phase composites (IPCs) *via* in-situ foaming that integrate stochastic polymeric foam with elastomeric gyroid lattices featuring robust interfacial integration and precisely controlled architecture and density profile. This hybrid design couples the high specific energy absorption of foam with the tunable stiffness and structural integrity of architected lattices, leading to synergistically improved mechanical performance that neither standalone constituent achieves. Introducing a density gradient to IPC enables spatially programmed deformation and gradient-governed load transfer. Under impact loading, the IPCs exhibit dynamic synergy beyond the response of each individual component, markedly reducing transmitted peak stress and acceleration while simultaneously increasing energy absorption at low strain levels. The gyroid lattice–foam IPCs offer a versatile strategy for designing lightweight structural materials that integrate load-bearing capacity with impact-mitigation capability.

Keywords: Polymer foam, Gyroid lattice, Interpenetrating phase composite (IPC), Additive manufacturing, Impact mitigation

1. Introduction

Many critical engineering applications demand lightweight materials capable of dissipating large amounts of energy while maintaining sufficient load-bearing capacity and structural integrity. Porous materials such as open or closed-cell polymeric foams are widely utilized across diverse industries—including automotive, aerospace, sports, and personal protection—owing to their ability to absorb and dissipate energy under impact and vibration at lightweight [1–6]. Their stochastic porous microstructure imparts several advantageous properties, including low density, high specific strength, high mechanical energy absorption, and effective thermal and acoustic insulation [3,6]. This energy absorption in polymeric foams primarily arises from the intrinsic viscoelasticity of polymer matrix, together with microstructural deformation mechanisms such as cell-wall bending, buckling, collapse, and fracture under loading. These mechanisms result in a characteristic stress–strain response featuring a plateau regime, during which the foam maintains nearly constant stress while accommodating large strains—typically a desired feature for impact and crash energy absorption [7–11]. However, inherently low modulus of these polymeric foams limits their load-bearing capability, motivating efforts to overcome this limitation by increasing the foam density [12], integrating different foam types [13], and adding high-performance reinforcing phases [14–16]. For instance, polymeric foams are integrated as low-density core materials in sandwich or hybrid composites, where the eventual composite system improves structural stability, stiffness-to-weight efficiency, multifunctionality, and impact energy absorption [17–20]. However, despite their high deformability, recoverability, and ease of fabrication, controlling their mechanical properties in polymeric foams remains challenging because their stochastic cellular microstructures arise from random void nucleation, growth, and coalescence during chemical blowing or gas expansion, rather than from deterministic patterning [6,7,11,21,22].

On the other hand, additive manufacturing (AM) enables precise fabrication of large-scale architected materials with complex, controllable topologies [23–28]. Due to this controllability, additively manufactured architected lattice structures are emerging as effective lightweight, energy-absorbing materials for impact mitigation and structural applications [28–31]. 3D-printed architected lattices such as octet-truss [32,33], honeycomb [34,35], and gyroid architectures [36,37] have demonstrated enhanced specific strength and stiffness while providing design-driven control over deformation and failure modes [38,39]. Among these, triply periodic minimal surface (TPMS)-based lattices, such as gyroids, feature continuous, smoothly curved surfaces that generate an interconnected network throughout the material. This nodal-free topology effectively reduces stress concentrations and mitigates sensitivity to manufacturing imperfections, such as voids and surface roughness [40,41]. Moreover, introducing structural gradient into

3D-printed elastomeric gyroid lattices enables spatially controlled deformation mode and tunable mechanical properties, including stiffness and energy absorption [28].

A key limitation of such lattice structures is their susceptibility to buckling, a structural instability that can induce abrupt large deformation or even catastrophic failure under applied load [32,33]. To overcome this, lattice-based composites are proposed—in which the porous lattice is infiltrated with a secondary phase to form interpenetrating-phase composites (IPCs). IPCs provide an effective and elegant pathway to couple lattice's high stiffness and strength with the host matrix's energy absorption capacity, while the matrix also stabilizes the lattice struts and prevents abrupt lattice buckling [13,29,42–44]. Studies on additively manufactured metallic body-centered cubic (BCC) trusses infilled with elastomeric matrix have shown high structural stiffness and enhanced energy absorption from the prolonged, smooth plateau stress [45]. However, IPCs with spatially tunable lattice architectures, such as structurally graded foam-lattice IPCs, remain largely unexplored for programming deformation patterns and thereby tailoring the overall mechanical response of the system. Also, the mechanical behavior of IPCs across quasi-static to dynamic loading regimes remain elusive, limiting their rational design and application in variable loading environments.

Here, we developed lattice-foam IPCs by integrating SLA 3D-printed elastomeric gyroid lattices, featuring tunable bulk relative densities (RDs) and spatial RD gradients, with soft polyurethane foam through an in-situ foaming process. We investigate how different RDs and RD gradient—enabled by graded architectures—govern deformation mechanisms and tailor the mechanical response across quasi-static to dynamic compression regimes. SEM and micro-computed tomography (micro-CT) analyses confirmed uniform foam infiltration and a well-bonded lattice–foam interface for the structural integrity of the interpenetrating architecture. Under compressive loads, the foam phase provides lateral constraint to the gyroid struts, enabling the hybrid composites to combine the stiffness tunability of architected gyroid lattices with the high specific energy absorption and large deformability of porous foams. Modulating the lattice RD spatially by introducing structural gradients, regulates the deformation spatially, delays instability, and promotes more effective load transfer during compression, ultimately enhancing specific energy absorption and dissipation. As a result, our IPC designs overcome the stiffness-energy absorption trade-off commonly observed in standalone foams and soft lattices more effectively, delivering enhanced stiffness, high energy absorption through sustained deformability and tunable mechanical responses. Importantly, the drop-weight impact tests further demonstrate markedly reduced transmitted stress and acceleration alongside increased dynamic energy absorption at low strains, confirming the outstanding impact-mitigation capability of the IPCs. This work establishes a versatile design framework for architected

lattice–foam IPCs that enables tailorable stiffness, enhanced energy absorption, and impact protection, highlighting their strong potential for advanced protective, automotive, and aerospace applications.

2. Design and Fabrication of Gyroid Lattice-Foam IPCs

We fabricated the elastomeric polymeric foams through a reactive foaming-and-curing process, in which the liquid precursor was mixed, cast into a mold, and allowed to expand and solidify. During curing, gas generated within the reacting matrix drives bubble nucleation and growth, leading to the formation of a stabilized cellular structure. The resulting foam consists of a 3D porous network with inherently irregular cell sizes, shapes, and wall thicknesses, characteristic of conventional polymeric foams (Fig.2a). The density of the foam is approximately ~121 ± 2 kg/m³ and it exhibits a soft texture with excellent post-compression recoverability. However, due to its highly porous and stochastic architecture, the foam alone provides limited resistance to mechanical deformation.

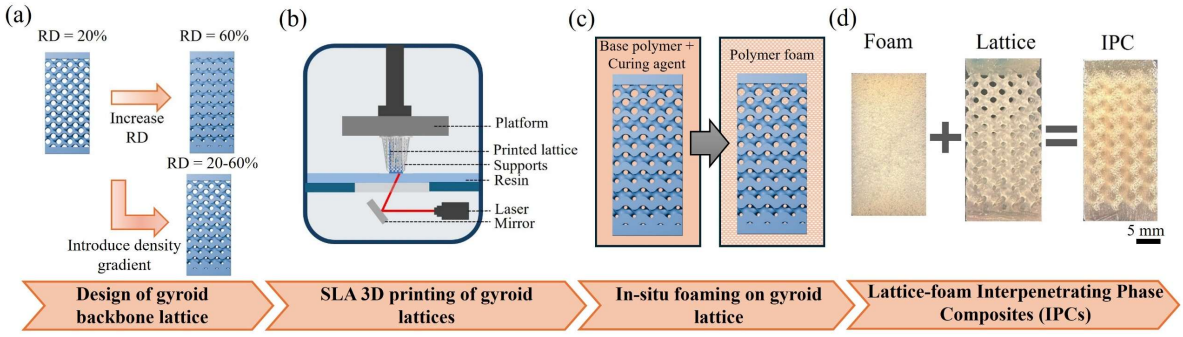

Figure 1. Schematic illustration of the fabrication process for lattice–foam interpenetrating phase composites (IPCs).

In contrast to the stochastic polymeric foams with random porosity, 3D-printed lattices provide a deterministic architecture whose mechanical response can be programmed through geometry[28,36,46]. We selected the gyroid topology (a TPMS structure) as the lattice skeleton for our IPCs due to its continuous, non-self-intersecting surface, which promotes more uniform stress distribution and delays localized collapse. Accordingly, a family of gyroid lattices was designed using the trigonometric approximation of the gyroid surface (Eq. 1).

$$\sin\left(\frac{2\pi}{a}\cdot x\right)\cos\left(\frac{2\pi}{a}\cdot y\right)+\sin\left(\frac{2\pi}{a}\cdot y\right)\cos\left(\frac{2\pi}{a}\cdot z\right)+\sin\left(\frac{2\pi}{a}\cdot z\right)\cos\left(\frac{2\pi}{a}\cdot x\right)=t \quad (1)$$

Here, a denotes the unit-cell size (a = 3 mm), and the lattice consists of 10 unit cells along the longer z-direction, giving a total height of 30 mm. The RD of the structure is controlled by varying the parameter t spatially within the lattice. Over the range $|t| \leqslant 1.5$, RD scales approximately linearly with t according to: $RD = 0.3325t + 0.501, |t| \leq 1.5$ [47,48]. Uniform-density lattices were generated by assigning a constant t to obtain RDs of 20%, 40%, and 60%. These RD values were selected based on SLA manufacturability

constraints: at very low RD, struts become too thin to print reliably, leading to discontinuous or broken features, whereas at very high RD, the reduced pore connectivity hinders drainage and removal of uncured resin trapped within the lattice. Graded lattices were created by defining t as a spatial field, $t = f(x, y, z)$; a linear profile $t = \lambda z$ was used to impose an RD gradient along the z-axis from 20% to 60% (Fig. 1a).

We fabricated all the gyroid lattices using a Formlabs Form 3 SLA printer with Elastic 50A resin (Fig. 1b). The fully cured resin provides high elongation (~160%) and an ultimate tensile strength of ~3.4 MPa, making it suitable for soft, deformable lattice structures. We first prepared STL files in PreForm, oriented with flat faces parallel to the build platform, and supported only on external surfaces to preserve internal features. After printing, we removed the printed part with the support structure from the building platform, cleaned in IPA using two 10 min sonication baths (fresh IPA for the second bath), air-dried for 3 h, post-cured at 70 °C for 10 min, and finally de-supported to obtain the target lattice architectures.

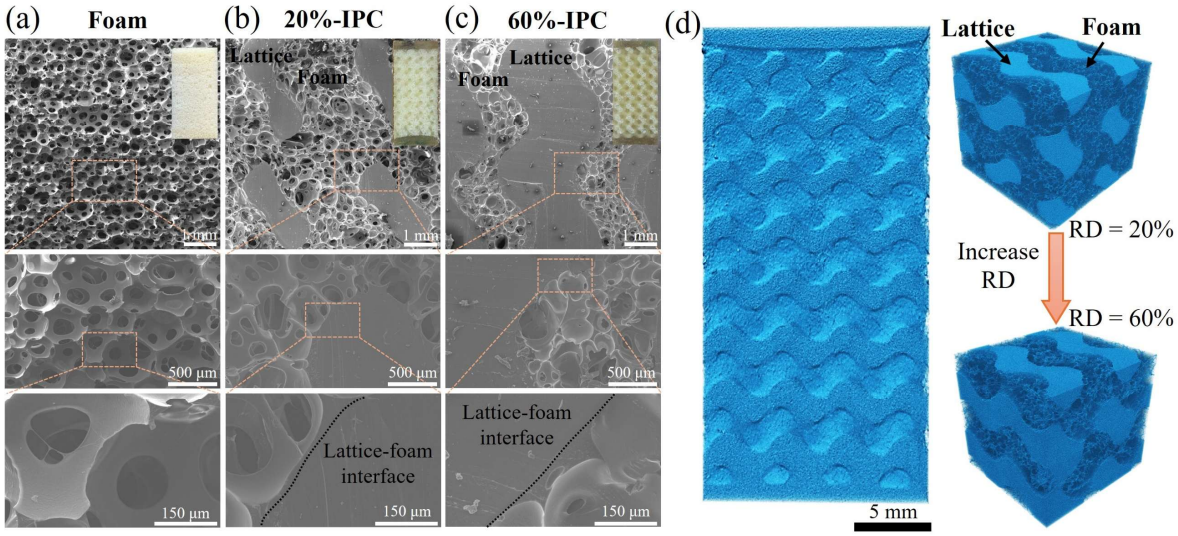

Figure 2. SEM images and corresponding digital photographs of **(a)** polymeric foam, **(b)** IPC with a 20%-lattice, and **(c)** IPC with a 60%-lattice at increasing magnifications. Dashed grey lines indicate the locations where the sample was sectioned and imaged. Dashed black lines mark the interfacial regions between the foam matrix and the lattice, demonstrating an excellent foam infiltration and interfacial bonding. **(d)** Micro-CT reconstructions of IPCs containing 20–60%-lattice, along with representative volumes showing lattice RD of 20% and 60% within the composite.

This design strategy of using SLA 3D printing to fabricate elastomeric gyroid lattices with diverse architectures, can enable a broad range of mechanical responses depending on the RDs as well as RD gradients (equation 1). Additionally, when integrated with a soft polymeric foam matrix, gyroid lattices are expected to establish a continuous load-bearing framework within the IPCs, thereby enhancing structural stiffness and regulating deformation, while the foam matrix contributes to improved energy absorption. To obtain such lattice-foam IPCs, the printed gyroid lattices with varying architectures were placed in a sealed container that defined the composite geometry (Fig.1c), and the foam precursor mixture was later

introduced to infiltrate the interconnected lattice and wet the internal surfaces, ensuring intimate interfacial contact between the two phases. Foaming and curing proceeded in situ within the confined architecture, producing a porous foam matrix that expanded to occupy the lattice pore volume. We ensured that the amount of foam precursor used was precisely measured to match the density of the standalone foam, thereby maintaining comparable porosity and composition. After ~60 min, we demolded the IPCs and removed the excess surface foam (Fig. 1d). The foam density, calculated from the lattice-to-composite mass gain and foam volume, averaged ~135 ± 12 kg/m³—slightly (11%) higher than the pure foam, due to the constrained bubble growth and enhanced gas retention—with no systematic variation across different gyroid RDs.

We performed a detailed SEM analysis to evaluate the structural integrity and interfacial quality in cross-sectional IPC specimens with two lattice volume fractions—20% and 60%—and included pure foam as a baseline (Fig. 2a–c). No clear trend in foam cell opening was observed across the specimens. Samples were sectioned to expose the foam and lattice regions, and the interfaces were examined across multiple magnifications. SEM images show a uniform, well-integrated microstructure: foam cells are tightly packed against the gyroid struts, with no observable voids, delamination, or interfacial debonding. The intimate contact between the gyroid strut surface and surrounding foam indicates strong interfacial compatibility and efficient load-transfer pathways, confirming that in-situ foaming yields continuous interpenetrating architecture in the IPCs. These observations were corroborated by micro-CT reconstructions (Fig.2d and Supplementary Video), which reveal fully infiltrated, defect-free internal structures. For graded lattices (RD = 20–60%), 3D reconstructions show a homogeneous architecture with smooth transitions in density, continuous gyroid connectivity, and uniform foam filling from the low-RD (20%) to high-RD (60%) regions (Fig. 2d). No unfilled zones, cracks, or interfacial separations were detected across any RD configuration, indicating that RD variation did not compromise resin infiltration or phase continuity. Collectively, SEM and micro-CT analyses validate the fidelity and robustness of our in-situ foaming fabrication route and establish that the IPCs are well-suited for systematic mechanical study and failure analysis.

3. Results and Discussion

3.1 Quasi-static Compression Mechanics of the IPCs

We performed uniaxial quasi-static compression tests on the standalone foam, gyroid lattices, and lattice–foam IPCs to elucidate their synergistic mechanical response, with emphasis on deformation modes, load-bearing capacity, and energy-absorption performance relative to the individual constituents. Figure 3a, b compares the nominal stress–strain responses of the polymeric foam and 3D-printed gyroid lattices. The foam exhibits the classic three-stage compression response of cellular solids: an initial linear regime dominated by cell-wall bending, a near-constant plateau associated with progressive cell collapse, and a densification stage characterized by a rapid stress increase as pores close (Fig. 3a). The loading–unloading

curves show pronounced hysteresis, arising from viscoelastic dissipation in polymer skeleton, accompanied by cell-wall bending, buckling/collapse, and frictional contact during foam compression and recovery [49]. In contrast, the 3D-printed pure gyroid lattices exhibit distinct mechanical responses, however they can be tuned by varying RD and RD gradients, arising from their deterministic periodic topology (Fig. 3a, b). At RD = 20%, the gyroid lattice shows a low initial modulus and a smooth, continuously increasing stress–strain response with only a weakly defined plateau. The modulus measured at 5% strain is 0.15 ± 0.03 MPa for the RD = 20% lattice, which is lower than that of the standalone foam (0.27 ± 0.01 MPa), but increases sharply with RD, reaching 1.94 ± 0.11 MPa at RD = 60% (Fig. 3c), highlighting strong RD-dependent stiffening of the lattice architecture. Consistent with this near-elastic structural response, the loading–unloading hysteresis is markedly narrower than that of the polymer foam, indicating reduced energy dissipation under similar quasi-static loading-unloading cycle (Fig. 3a). Notably, the mechanical tests on lattices with different RDs are terminated at different maximum strains, selected based on post-deformation visual inspection to avoid strut fracture at each RD. Within these strain limits, the lattices remain damage-

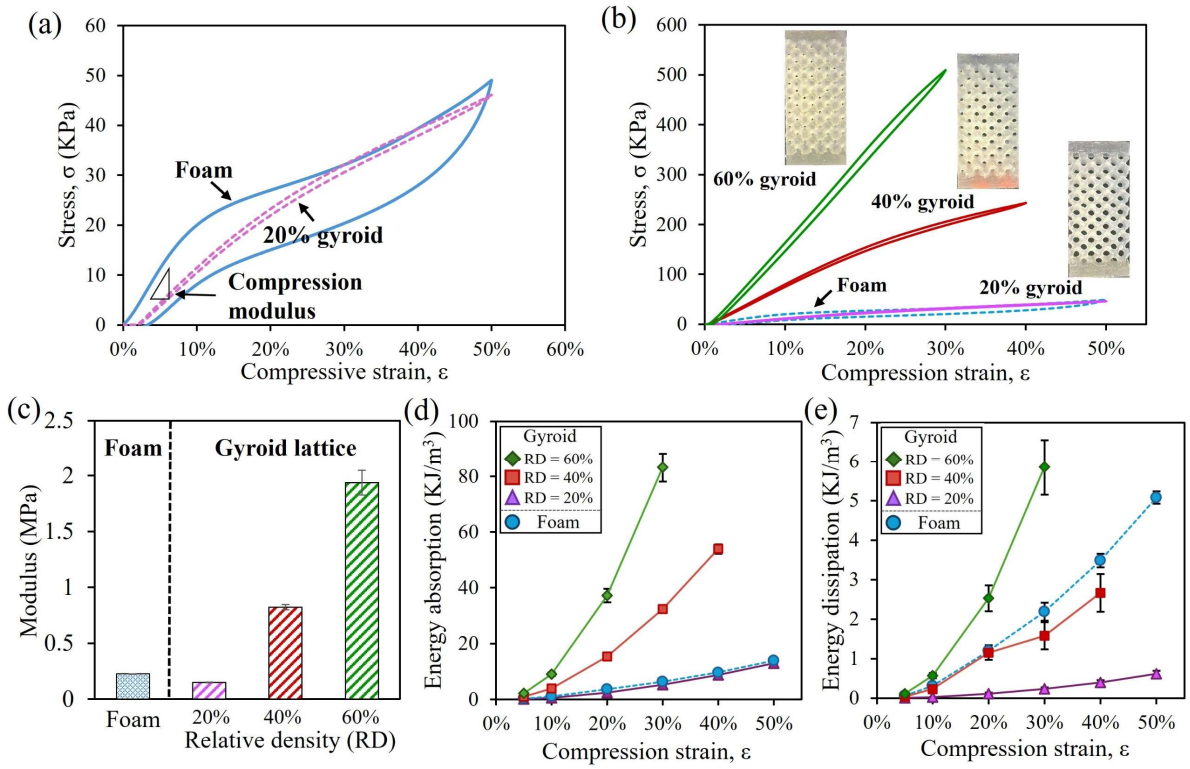

Figure 3. (a) Compressive stress–strain responses of the standalone foam and the pure gyroid lattice with RD = 20%. **(b)** Comparison of compressive stress–strain responses of gyroid lattices with RD = 20%, 40%, and 60%, in comparison with the standalone foam. **(c)** Compressive modulus of the foam and gyroid lattices as a function of RD. **(d)** Energy absorption and **(e)** energy dissipation of the foam and gyroid lattices. Error bars represent the standard deviation of three replicates (n = 3). Lines are included only as visual guides and do not represent fitted curves.

free, and unloading shows full recoverability, confirming viscoelastic bending/buckling-dominated and largely reversible deformation without strut damage.

The gyroid lattices also demonstrate pronounced RD-dependent energy absorption and dissipation (Fig. 3d,e), where the energy absorption is evaluated from the area under the loading stress–strain curves while the energy dissipation is evaluated from the area enclosed by the loading-unloading curves. Across the tested strain range (5–50%), the RD = 20% lattice exhibits energy absorption comparable to that of the standalone foam (Fig. 3d), but at approximately twice the mass of standalone foam, resulting in reduced mass-normalized performance. As RD increases, the lattices sustain higher stresses at a given strain and absorb more energy, as indicated by the larger area under the loading curve (Fig. 3b), consistent with a transition from bending-dominated deformation toward a mixed bending–stretching mode [48,50,51]. Energy dissipation (Fig. 3e) remains high for the standalone foam, even exceeding that of the RD = 40% gyroid despite its ~4-fold lower mass. This behavior is attributed to the foam's heterogeneous cellular microstructural morphology, which promotes distributed viscoelastic deformation and frictional dissipation

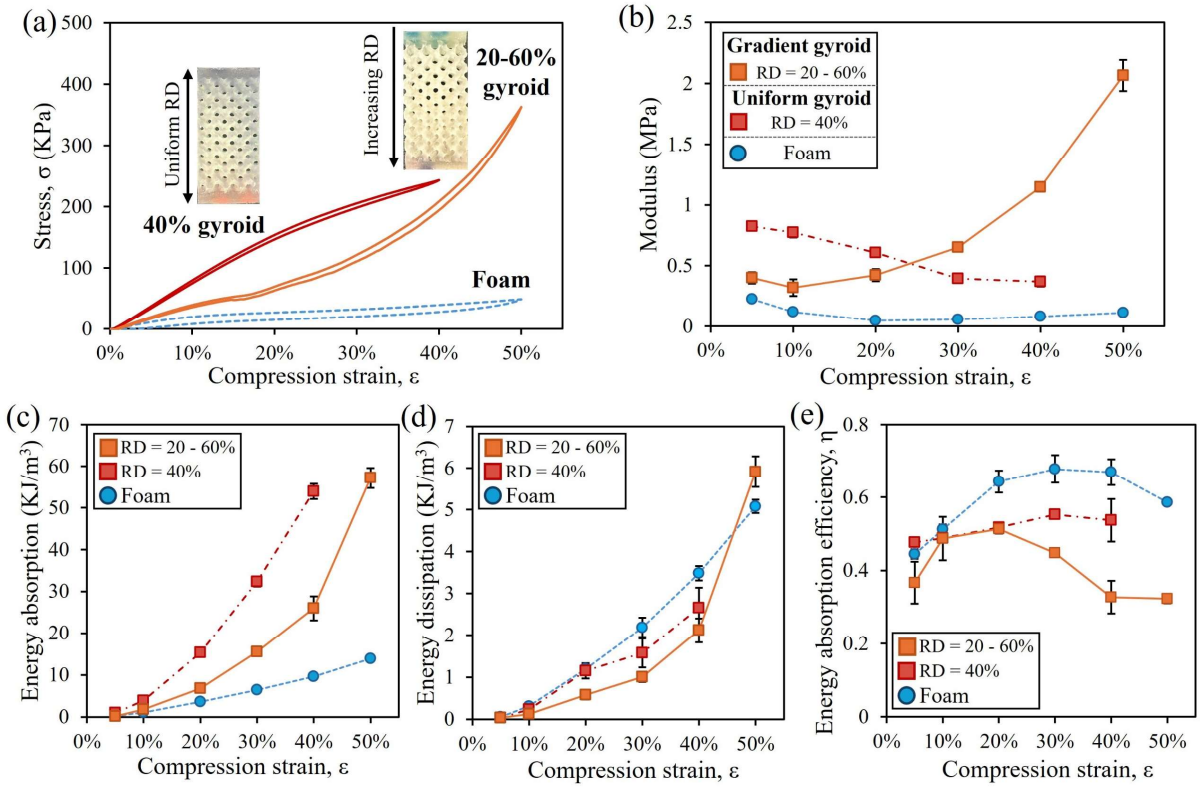

Figure 4. (a) Compressive stress–strain responses of the polymeric foam and gyroid lattices with uniform and gradient RDs. Evolution as a function of applied strain for **(b)** compressive modulus, **(c)** energy absorption and **(d)** energy dissipation characteristics **(e)** energy absorption efficiency for gyroid lattices with uniform and gradient density configurations relative to the polymeric foam. Error bars represent the standard deviation of three replicates (n = 3). Lines are included only as visual guides and do not represent fitted curves.

across length scales (Fig. 2a). In contrast, the gyroid lattices show progressively higher energy dissipation with increasing RD across the tested strain range as higher RD architecture engages more material enabling higher viscoelastic dissipation at a given strain.

To further program the deformation sequence and enable spatially graded mechanical behavior, we introduced a linear density gradient (RD = 20–60%) along the loading direction of the gyroid, creating a graded gyroid that had a similar bulk density as the RD = 40% gyroid. The stiffness gradient emerging from the density gradation produces a nonlinear stiffening stress–strain response under compression (Fig. 4a). This behavior arises from progressive local strain concentration within the graded architecture: deformation initially accumulates in the low-RD region, where local densification occurs earlier, and subsequently redistributes toward higher-RD regions at larger global strains (Fig. 6c). Consistently, the modulus of the graded gyroid increases with strain as sequential densification engages progressively denser regions of the architecture (Fig. 4b). In contrast, the uniform RD = 40% lattice, with similar bulk density shows a reduction in modulus before densification, associated with spatially uniform deformation governed by simultaneous strut bending and buckling (Fig. 6b).

For energy absorption (Fig. 4c), both the uniform (RD = 40%) and the graded (RD = 20-60%) gyroids absorb more energy than the standalone foam as strain increases, owing to their higher load-bearing capacity during compression. The graded lattice exhibits lower absorbed energy at small strains because its initial response is governed by the compliant low-RD region. However, the graded architecture remains mechanically stable even at larger strains, whereas the uniform lattice develops strut damage and instability at such high strain, requiring earlier termination of the test ($\varepsilon = 40\%$ for the uniform lattice vs. $\varepsilon = 50\%$ for the graded lattice). As a result, when evaluated over the larger accessible strain window, the graded gyroid accumulates greater total absorbed energy than the uniform gyroid. The energy dissipation follows a similar trend (Fig. 4d). At the same strain level, the graded gyroid generally dissipates less energy than the uniform RD = 40% gyroid since its early-stage deformation is governed by the low-RD region. However, as discussed, its improved deformation stability enables sustained energy dissipation up to higher strains, resulting in greater total dissipated energy over the full loading range.

Energy absorption efficiency (EAE) is an important parameter for evaluating cellular materials performance because it relates the absorbed energy to the maximum stress required to achieve a given strain, thereby reflecting how effectively a material absorbs energy without imposing excessive transmitted stress under different loading conditions [52–54]. The EAE is defined as:

$$\eta = \frac{\int_0^{\varepsilon} \sigma(\varepsilon) d\varepsilon}{\sigma_{max}\varepsilon} \quad (1)$$

where σ_{max} denotes the maximum stress reached before the specified strain and ε is the strain applied. Compared to the standalone foam, both uniform and graded gyroids exhibit lower EAE with increasing strain (Fig. 4e), mainly because their stress–strain responses deviate from the ideal foam's plateau-like response (Fig. 4a). The progressive stress increase during lattice deformation raises the maximum stress, thereby reducing the EAE despite increased total energy absorption [38,44]. When the applied strain exceeds 20%, the efficiency of the graded gyroid decreases further and becomes lower than that of the uniform gyroid, which can be attributed to localized densification (Fig. 6 b,c), that sharply increases the stress level in the graded sample without a proportional increase in absorbed energy.

Overall, stochastic foam and deterministic gyroid architectures exhibit complementary attributes: the foam exhibits high specific energy absorption and dissipation, whereas gyroid lattices show higher, RD-tunable stiffness and architecturally controlled deformation response. These trends motivate the integration of foam with gyroid lattices in an IPC framework, coupling foam-like energy absorption and dissipation with lattice-derived stiffness, structural stability, and RD-tunable deformation control. In addition, introducing a density gradient within the gyroid phase provides a further design lever to locally tune the foam-to-lattice ratio and deformation sequence, thereby tailoring the effective bulk response.

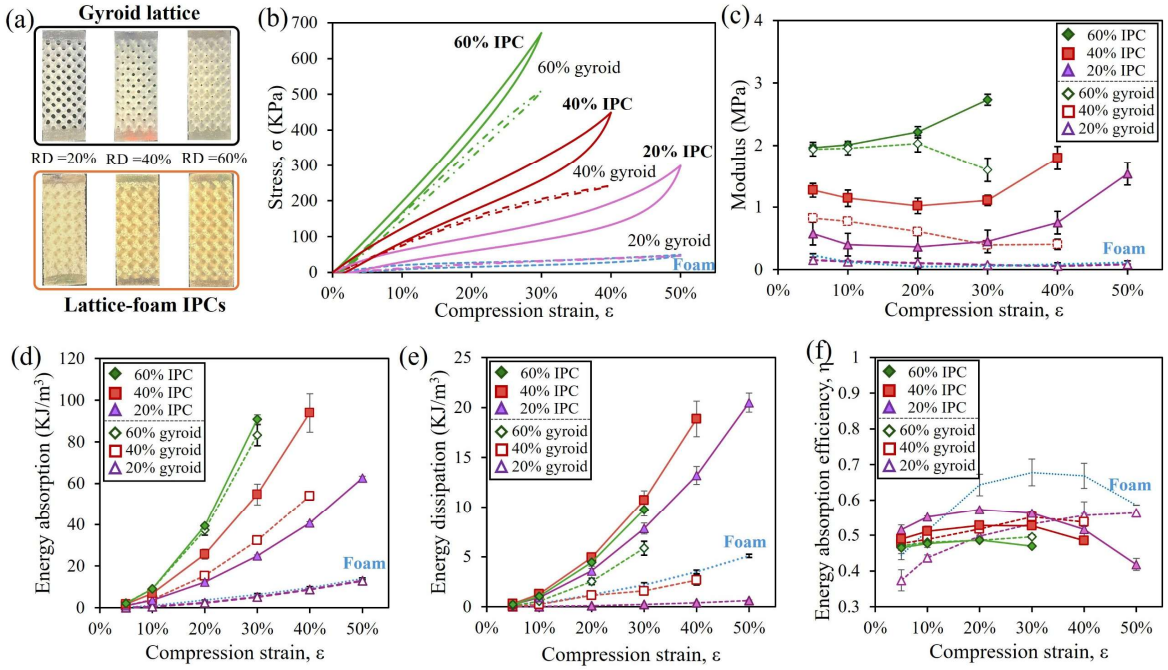

Figure 5. (a) Lattice–foam IPCs incorporating gyroid lattices with RDs of 20%, 40%, and 60%. **(b)** Compressive stress–strain curves of IPCs and gyroid lattices. **(c)** Comparison of compressive modulus, **(d)** total energy absorption, **(e)** energy dissipation and **(f)** energy absorption efficiency for IPCs, gyroid lattices of corresponding RDs, and the polymeric foam. Error bars represent the standard deviation of three replicates (n = 3). Lines are included only as visual guides and do not represent fitted curves.

Building on these complementary mechanical behaviors, we fabricated a series of lattice–foam IPCs by integrating polyurethane foam into 3D printed gyroids through in-situ foaming. We fabricated 4 IPC variants comprising uniform gyroid architectures with RDs of 20%, 40%, and 60% (Fig. 5a), as well as a graded gyroid architecture spanning 20–60% RD (Fig. 6a). Relative to the standalone constituents, all IPCs sustained higher stresses within the plateau-like region and exhibited enlarged loading–unloading hysteresis, indicating enhancement in both structural stiffness as well as energy dissipation (Fig. 5b). In the IPCs, the gyroid network serves as a continuous load-bearing skeleton, whereas the foam phase occupies the lattice pores, mechanically coupling the neighboring struts. This critical coupling not only improves the load transfer between struts but also provides lateral support to struts, preventing premature strut bending and buckling within the gyroid framework. This increases the initial modulus of the IPC system beyond that of either standalone constituent. As compression proceeds, the confined foam contributes to additional dissipation through viscoelastic deformation and cell-wall collapse, while restraining excessive strut bending and buckling. These synergistic mechanisms stabilize the deformation of low-RD lattices and transform their strain-softening, instability-prone response into a more stable, strain-stiffening behavior (Fig. 5c). This enhancement is most pronounced in the low-RD IPCs, where the compliant lattice benefits most strongly from foam-mediated support. For example, at 50% strain, the standalone RD = 20% gyroid has a modulus of only 0.08 ± 0.01 MPa, whereas the corresponding IPC reaches 1.54 ± 0.03 MPa, representing an enhancement greater than 1800% with a ~50% mass increase (Fig. 5c). At higher relative density (RD = 60%), the modulus enhancement is more modest but still substantial, increasing by ~69% from 1.62 ± 0.20 MPa for the standalone gyroid to 2.73 ± 0.10 MPa for the IPC at 30% strain, while adding only ~10% mass.

Energy absorption and dissipation exhibit similar RD-dependent significant enhancements in the IPCs (Fig.5 d,e). Relative to the standalone RD = 20% gyroid, the corresponding IPC increases total energy absorption by 385%, whereas the RD = 60% IPC shows a modest 9% increase (Fig. 5d). For energy dissipation, RD = 20% IPC exhibits a 336% increase relative to its standalone gyroid, compared with a 78% increase for the RD = 60% IPC (Fig. 5e). Moreover, at low strains, the IPCs exhibit higher EAE than the corresponding standalone lattices, indicating that foam integration effectively increases energy uptake without a comparable rise in peak stress. This improvement is critical for impact mitigating materials and structures, where high energy absorption must be achieved while limiting the stress transmitted to protected components or users [11,55]. This lower-strain efficiency enhancement is attributed to foam-mediated lateral constraint of the sparse low-RD gyroid framework, which stabilizes strut deformation and increases absorbed energy without a proportional increase in peak stress. At larger strains, however, foam compression and lattice densification progressively elevate the stress level, reducing the normalized efficiency and causing the EAE to fall below that of the standalone lattices. This efficiency benefit becomes

less pronounced with increasing RD, as the response is increasingly governed by the denser gyroid framework.

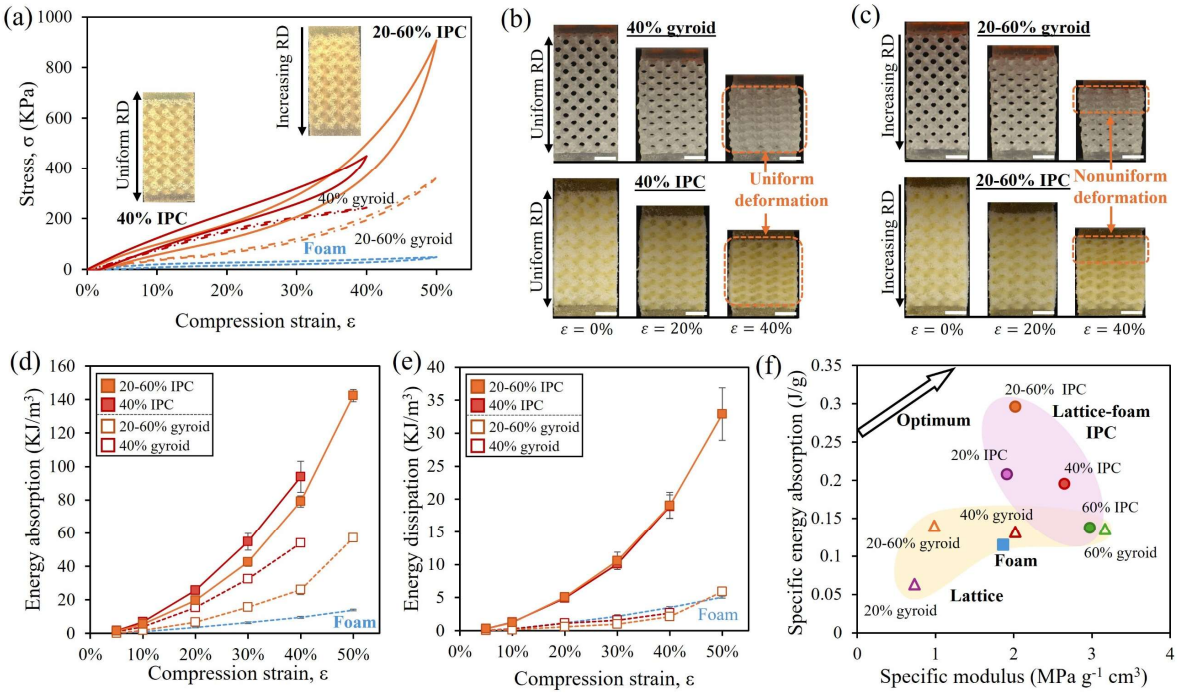

Figure 6. (a) Representative photographs and compressive stress–strain curves of IPCs incorporating gyroid lattices with uniform and graded RD. Deformation sequences at increasing compressive strain showing the distinct compression modes of **(b)** uniform RD = 40% gyroid lattices and the corresponding IPCs, and **(c)** graded RD = 20–60% gyroid lattices and the corresponding IPCs. Comparison of **(d)** energy absorption and **(e)** energy dissipation characteristics of the IPCs relative to the standalone gyroid lattices and foam. Error bars represent the standard deviation of three replicates (n = 3). Lines are included only as visual guides and do not represent fitted curves. **(f)** Ashby plot of specific modulus versus specific energy absorption for the foam, lattice and IPCs.

Introducing a density gradient within the gyroid phase further tailors the deformation behavior and enhances IPC performance relative to uniform-RD architecture (Fig. 6a). The foam-to-lattice ratio gradient along the loading direction promotes sequential deformation in the graded IPC (Fig. 6c), in contrast to the spatially uniform deformation observed in the uniform RD = 40% IPC (Fig. 6b). At lower strain levels, deformation is concentrated in the compliant low-RD region, where the gyroid framework and interpenetrated foam deform cooperatively and provide early-stage energy dissipation. As compression proceeds, local compaction of the low-RD region increases its resistance, causing deformation and load transfer to become progressively shared with higher-RD regions. This deformation sequence engages stiffer load-bearing segments while maintaining foam-assisted dissipation throughout the structure. This gradient architectural effect is reflected in the mechanical performance. At 40% strain, foam interpenetration increases the modulus of the uniform gyroid (RD = 40%) architecture by 343%, whereas the graded RD =

20–60% architecture shows a 136% increase under the same condition. Despite this smaller relative stiffness gain, the graded IPC achieves a 149% increase in total energy absorption, compared with 74% for the uniform RD = 40% IPC, highlighting the added benefit of density grading within the IPC architecture (Fig. 6d). Energy dissipation shows a related trend. While the graded standalone gyroid dissipates less energy than the uniform RD = 40% gyroid at the same global strain (Fig. 4d), foam interpenetration compensates for this difference, enabling the graded IPC to reach moderately higher dissipation relative to the uniform RD = 40% IPC (Fig. 6e). This result highlights that the optimal spatial tailoring of the backbone gyroid architecture is critical for fully exploiting the performance enhancements enabled by foam interpenetration in foam–gyroid lattice IPC systems.

Figure 6f presents an Ashby plot of specific modulus versus specific energy absorption for the standalone foam, gyroid lattices, and lattice–foam IPCs. These mass-normalized metrics are critical for practical energy-absorbing structures, where performance is often constrained by weight. High specific modulus reflects load-bearing capacity and structural stability per unit mass, whereas high specific energy absorption indicates efficient energy uptake without excessive weight penalty. Tuning the RD of standalone gyroids increases specific modulus but provides only limited improvement in specific energy absorption, revealing a stiffness–energy absorption trade-off. The stochastic foam shows high specific energy absorption but low stiffness. Thus, neither constituent alone, nor RD tuning of standalone lattices, can simultaneously maximize both properties. In contrast, lattice–foam IPCs shift upward and to the right in the Ashby space, achieving concurrent gains in specific modulus and specific energy absorption. This shift indicates that foam interpenetration complements each constituent phases and activates coupled deformation mechanisms: the gyroid skeleton provides load-bearing continuity, while the confined foam stabilizes strut deformation and dissipates energy. By decoupling stiffness enhancement from the usual energy-absorption penalty, the IPCs access an otherwise inaccessible property space, not only effectively overcoming the conventional stiffness–energy absorption trade-off but also the density-dependent scaling limitation of the standalone architectures. Notably, the graded IPC exhibits the most pronounced enhancement, significantly surpassing the expected rule-of-mixtures response through deformation programming enabled by the spatially graded lattice architecture. This result further shows that IPC performance is governed not only by the overall RD, but also by its spatial distribution, thereby expanding the design space beyond conventional bulk RD tuning.

3.2 Impact Mechanics of the IPCs

To evaluate the dynamic mechanical synergy between the lattice and foam phases and the resulting impact-mitigation performance, we performed drop-weight impact tests on standalone gyroid lattices and lattice–foam IPCs at a fixed impact energy of 5 J with an impact velocity of 1.33 m/s (Fig. 7a). Unlike

strain-controlled quasi-static compression, drop-weight loading imposes a prescribed impact energy and allows the specimen response to evolve according to its intrinsic architecture and material properties. This approach enables direct comparison of key impact metrics, including maximum strain, peak stress, acceleration attenuation, and absorbed impact energy, across different architectures.

Upon impact, the standalone gyroid lattices deform primarily through strut bending and yielding, followed by buckling and densification. Their periodic architecture enables relatively homogeneous deformation under dynamic compression (Fig. 7b,d). Increasing RD enhances the stiffness and load-bearing capacity of the lattice backbone; therefore, under fixed impact energy, denser gyroid architectures exhibit lower maximum strain and reduced peak stress (Fig. 8c,d). This trend reflects improved deformation control and impact-load attenuation rather than premature structural collapse.

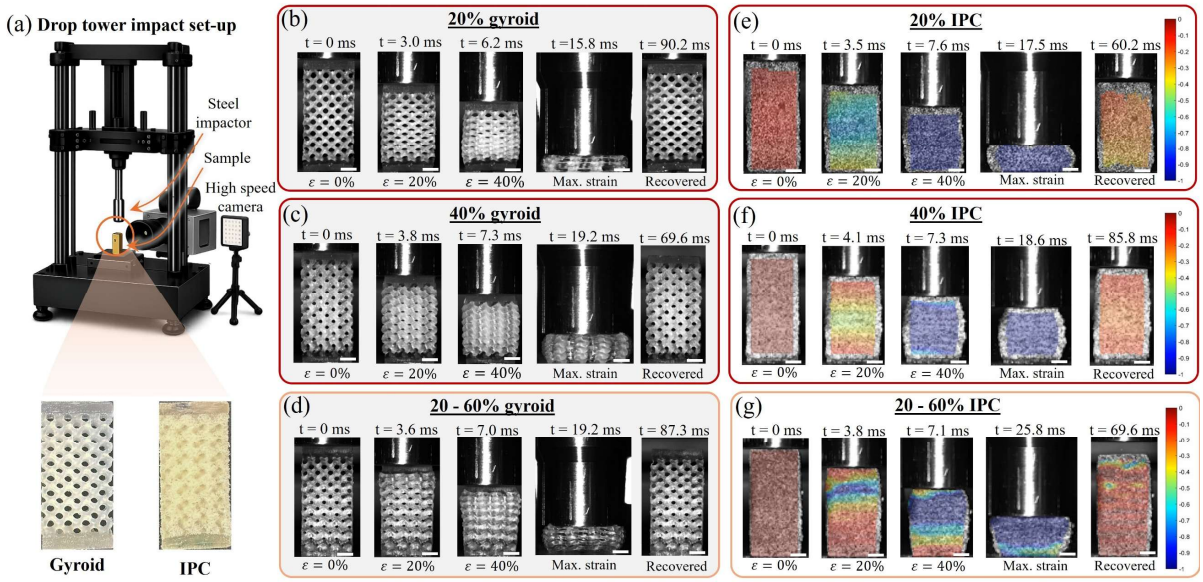

Figure 7. (a) Schematic diagram of the drop-weight testing setup. High-speed image sequences of **(b)** the uniform RD = 20%, **(c)** RD = 40% gyroid lattice and **(d)** graded RD = 20–60% gyroid lattice during impact at the indicated times/strains. Digital image correlation (DIC) maps showing the strain fields of the corresponding IPCs at the indicated times/strains: **(e)** 20% IPC, **(f)** 40% IPC and **(g)** graded 20–60% IPC (scale bar: 5 mm).

Foam interpenetration substantially modifies the dynamic response of the gyroid architectures, consistent with the quasi-static compression results. The impact stress–strain curves show that, compared with the standalone lattices, the IPCs develop higher stresses at smaller compressive strains, indicating stronger early-stage impact resistance and effective dynamic mechanical coupling between the lattice and foam phases (Fig. 8a). The enlarged hysteresis in the IPCs further suggests the activation of additional energy-dissipation pathways during impact. As a result, foam interpenetration reduces the maximum compressive strain across all RDs (Fig. 8c), demonstrating that the coupled lattice–foam architecture

constrains excessive deformation, thereby premature densification under the same impact energy. This deformation suppression is accompanied by a reduction in peak transmitted stress, a key metric for impact-mitigation systems because it represents the maximum load delivered to the protected component and often governs damage or injury thresholds (Fig. 8d). The effect is most pronounced for the RD = 20% architecture, where the standalone lattice is highly compliant and susceptible to large deformation, eventually leading to structural densification (Fig. 8a). In this low-RD architecture, the foam laterally supports the slender struts, suppresses localized buckling and premature densification, and promotes cooperative deformation between the two interpenetrating phases. Consequently, the peak stress decreases from 10.2 ± 0.4 MPa for the standalone gyroid to 6.5 ± 0.3 MPa for the IPC, corresponding to a 37% reduction. As RD increases, the lattice backbone becomes intrinsically stiffer and more stable, reducing the relative contribution of the foam phase to peak-stress attenuation; accordingly, the reduction decreases to 7% and 6% for the RD = 40% and RD = 60% IPCs, respectively.

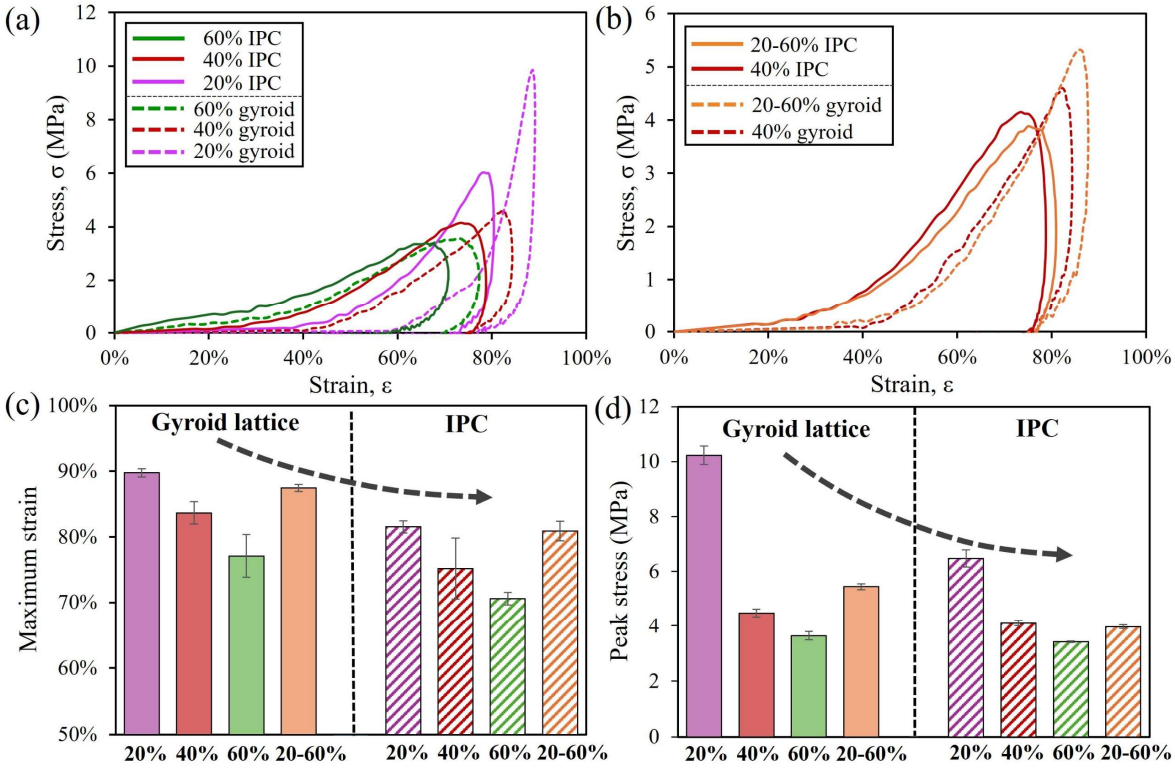

Figure 8. Impact compressive stress–strain curves of **(a)** uniform gyroid lattices and corresponding IPCs with different RDs and **(b)** graded RD = 20–60% gyroid lattices and the corresponding IPCs. Foam interpenetration leads to **(c)** lower maximum strain and **(d)** lower peak stress in IPCs than standalone gyroid lattices. Error bars represent the standard deviation of three replicates (n = 3).

The DIC-derived strain fields provide direct evidence for this mechanism by showing that foam interpenetration promotes a spatially distributed strain field within the IPCs (Fig. 7b,d). Rather than deforming as an unconstrained stochastic foam, the foam phase is confined by the continuous gyroid

backbone, while the lattice is laterally stabilized by the surrounding foam. This mutual constraint delays localized instability and supports the observed reductions in both maximum strain and peak transmitted stress. Upon unloading, both the standalone lattices and IPCs show nearly complete shape recovery, consistent with non-catastrophic deformation and viscoelastic rebound of the polymeric constituents (Fig. 7c,e).

The acceleration–time responses provide a complementary measure of impact-mitigation performance (Fig. 9a). Reducing peak acceleration is essential for protective materials because short-duration acceleration spikes, often associated with abrupt densification and rapid stress rise, can transmit damaging impulse loads to protected components or biological tissues [56,57]. In the standalone uniform gyroid lattices, increasing RD reduces peak acceleration and broadens the deceleration history, indicating more stable momentum transfer over a longer time window. For example, peak acceleration decreases from 438 m s^{-2} at RD = 20% to 128 m s^{-2} at RD = 60% (Fig. 9a). This trend is accompanied by greater energy uptake at lower strains, as the stiffer lattice backbone engages earlier and sustains higher loads during compression (Fig. 8a).

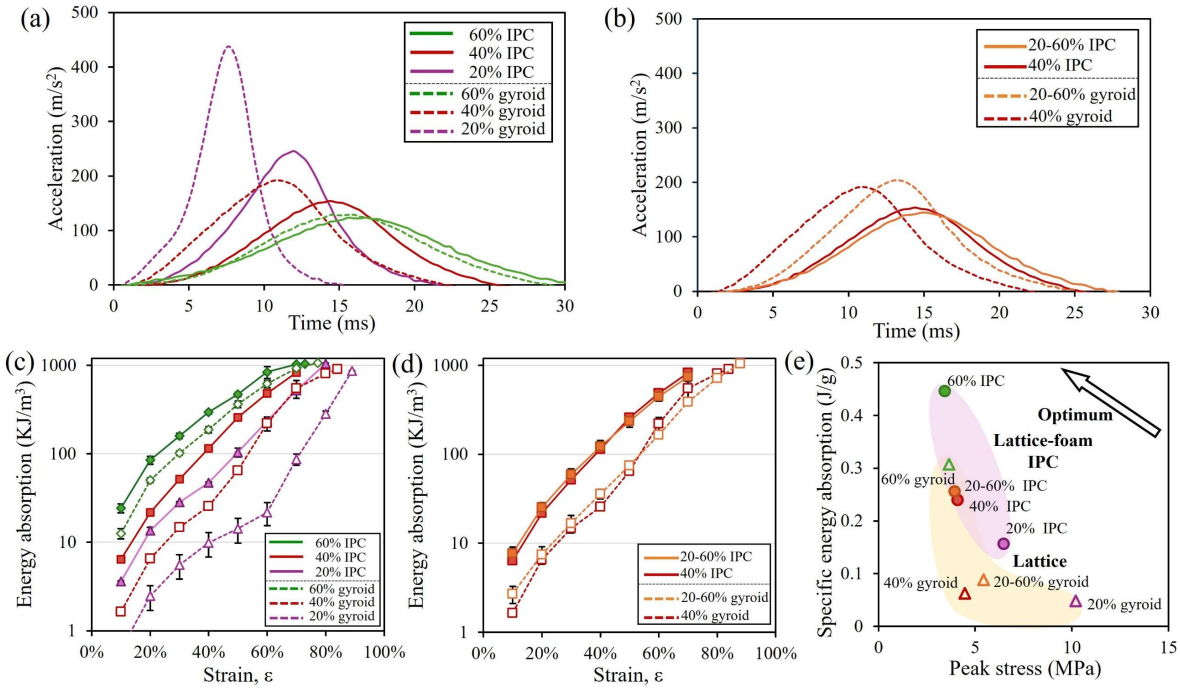

Figure 9. Acceleration–time histories under impact for the **(a)** uniform standalone gyroid and its IPC counterpart and **(b)** graded standalone gyroid and its IPC counterpart. **(c)** Energy absorption versus compressive strain for the **(c)** uniform standalone gyroid and the corresponding IPC and **(d)** graded standalone gyroid and the corresponding IPC. Error bars represent the standard deviation of three replicates (n = 3). Lines are included only as visual guides and do not represent fitted curves. **(f)** Ashby plot of specific impact energy absorption at 40% compressive strain versus peak transmitted stress for all architectures.

Foam interpenetration further moderates the acceleration response, with the strongest benefit observed at low RD. For the RD = 20% architecture, peak acceleration decreases from 438 to 236 m s^{-2}, corresponding to a 46% reduction, whereas the RD = 60% architecture changes only slightly from 128 to 124 m s^{-2}, or approximately 3% (Fig. 9a,b). This RD-dependent effectiveness arises from the distinct deformation mechanisms of each architecture: the low-RD lattice is highly compliant and prone to early localized collapse and rapid densification, whereas the high-RD lattice is already sufficiently stiff and stable to dominate the early-stage response. By providing distributed constraints, additional load paths, lateral strut stabilization, and viscoelastic energy dissipation, the foam phase delays abrupt densification and suppresses acceleration transients, particularly in the low-RD IPC. Consistently, foam interpenetration shifts energy absorption toward the early strain regime, with the RD = 20% IPC achieving the highest energy absorption at low strains (Fig. 9c). For example, at 40% strain, energy absorption increases from 9.85 ± 3.05 KJ/m^3 to 46.93 ± 0.9 KJ/m^3, corresponding to an approximately 376% increase.

Density grading further reshapes the deceleration response by altering when and where the dominant resistance develops during impact. In the standalone graded gyroid, deformation first localizes within the compliant low-RD region, delaying the onset of the major acceleration peak (Fig. 7f and Fig. 9b). As impact deformation proceeds, strain localization and densification extend toward the stiffer high-RD region, where the rapidly increasing resistance produces a delayed deceleration pulse. Consequently, the graded lattice can exhibit a higher peak acceleration than the uniform counterpart, despite shifting the peak to a later time (Fig. 9b). Foam interpenetration markedly modifies this response. Unlike the more distributed strain field observed in the uniform IPCs (Fig. 7e), the graded IPC retains a gradient-guided deformation pattern, with the DIC strain fields showing progressive local strain evolution from the low-RD region toward the high-RD region (Fig. 7g). This behavior indicates that foam interpenetration preserves the programmed deformation sequence of the graded gyroid backbone while suppressing abrupt localization and premature densification. As a result, the delayed acceleration spike is suppressed, and the graded IPC shows a lower peak acceleration and broader acceleration–time history (Fig. 9b). Notably, foam interpenetration brings the impact response of the graded IPC closer to that of the uniform IPCs, demonstrating that the foam phase mitigates the acceleration penalty associated with graded densification while preserving the deformation-control benefits of the gradient.

The overall impact-mitigation performance is summarized by plotting specific energy absorption at 40% compressive strain against peak transmitted stress (Fig. 9e). Movement toward the upper left represents the preferred combination of higher mass-normalized energy absorption and lower transmitted load. The fixed strain of 40% enables direct comparison across all architectures. Under the present drop-weight condition, the total absorbed energy is bounded by the imposed impact energy and the test endpoint; therefore, the

critical distinction among designs is how efficiently energy is absorbed at early strains and what peak stress is required to achieve that absorption. In this performance space, IPC formation shifts the response toward the upper left by simultaneously increasing early-strain energy absorption and reducing peak transmitted stress. This benefit is most pronounced at low RD and diminishes with increasing RD, as the denser lattice backbone increasingly governs the response.

Together, these results demonstrate that foam interpenetration and density gradation act as complementary design strategies for impact mitigation. Foam interpenetration introduces distributed constraint, lateral strut stabilization, additional load paths, and viscoelastic dissipation, which suppress abrupt densification and reduce transmitted acceleration and stress. Density grading further controls the spatial progression of deformation, extending the deceleration process and promoting more gradual momentum transfer. By combining these effects, lattice–foam IPCs decouple energy absorption from transmitted load, enabling lightweight architected materials that dissipate impact energy efficiently while limiting the mechanical impulse delivered to protected personnel and structures.

4. Conclusion

This study demonstrates that gyroid lattice-foam IPCs provide a robust and versatile route to overcome the intrinsic trade-offs that limit conventional cellular and architected materials for load bearing and impact mitigation applications. Polymeric foams exhibit high specific energy dissipation but low stiffness, whereas gyroid lattices provide RD-dependent stiffness and load-bearing capacity but comparatively limited dissipation. Integrating these phases yields synergistic performance that cannot be achieved by either constituent alone. For uniform gyroid lattices, mechanical response is readily tuned through relative density, and foam interpenetration further elevates performance by providing lateral constraint, stabilizing strut deformation, delaying buckling, and increasing energy absorption and hysteretic dissipation. These benefits are most pronounced in low-density lattices, where the foam plays a dominant role in suppressing localized instability and moderating densification-driven transients. Incorporating a density gradient along the loading direction further expands the attainable response space by promoting spatially programmed deformation and more effective load redistribution as crushing progresses. Under impact loading, the IPCs exhibit substantially reduced peak transmitted stress and peak acceleration together with enhanced early-strain energy absorption, indicating improved impact-mitigation capability and more controlled deceleration. Overall, gyroid lattice–foam IPCs emerge as a scalable platform for designing lightweight, high-performance energy-absorbing materials, offering tunable stiffness, an extended plateau regime, controlled densification, and superior impact attenuation. By strategically leveraging the rapidly advancing capabilities of additive manufacturing, IPCs offer unprecedented design flexibility for developing next-

generation aerospace structures, automotive crashworthy components, and advanced personal protective systems.

5. Materials and Methods

The polymeric foam phase was prepared using a flexible polyurethane casting foam (PolyFoam F-5, Polytek Development Corp.), mixed at a 1A:1B ratio by weight, poured into the molds, and allowed to cure at room temperature for 60 min before demolding. Gyroid lattice samples with uniform RDs of 20%, 40%, and 60%, as well as gradient-density structures—with the bottom region had RD 20% and the top region had RD 60%—were fabricated using a Formlabs Form 3 SLA printer with Elastic 50A resin. All 3D-printed lattice structures were rectangular prisms in shape with a 15 mm × 15 mm square base and 30 mm height. We produced lattice-foam IPCs by in-situ foaming using PolyFoam F-5. The printed gyroid scaffolds were placed into molds, and a two-part foam precursor was mixed, poured into the structures, and allowed to expand and cure for 1 h at room temperature.

We performed scanning electron microscopy (SEM) using Phenom XL Desktop SEM on sputter-coated cross-sections to thoroughly examine the microscale foam–lattice interfaces and strut morphology. Micro-computed tomography (micro-CT; Rigaku CT Lab HX-130) was used to verify complete foam infiltration and to characterize the internal architecture of both uniform and graded structures.

We performed the quasi-static compression tests on a Shimadzu AGS-J universal testing machine at a strain rate of 0.01 s^{-1} up to 50% engineering strain. Engineering strain was calculated from actuator displacement normalized by sample height, and nominal stress was obtained by dividing the measured load by the sample's cross-sectional area. For dynamic impact tests, we used an Instron CEAST 9350 drop-weight impact system equipped with a flat-tup striker. A fixed impact kinetic energy level of 5J was selected for all tests based on preliminary trials conducted at three distinct energy levels. All the impact experiments used the same sample nominal dimensions as in quasistatic experiments (15 mm × 15 mm × 30 mm). The impactor mass was 5.67 kg, and the impact velocity was obtained as 1.33 m/s for the 5J of kinetic energy. Force, displacement, and energy were recorded over time using the CEAST DAS 8000 Junior data acquisition system, at a sampling rate of 500 kHz. We employed high-speed imaging, using Photron FASTCAM Nova S6 camera, equipped with a Nikon AF-S NIKKOR 105mm lens, to capture the impact at a frame rate of 12,000 frames per second. The schematic illustration of the set-up is shown in Figure 7a. The automated trigger system relied on detecting a load increment, which introduced a delay in capturing the initial contact event for the soft samples. Therefore, the true impact duration and displacements were extracted from high-speed video footage, and these corrected values were used to update the force-displacement and energy-time datasets. Then the engineering strain was computed by normalizing the corrected displacement by the initial height of the lattice structure, while stress values were obtained by

dividing the measured force by the cross-sectional area of the sample. We adopted the same protocol across all tested samples, enabling direct comparison of stress–strain behavior, peak stress, acceleration response, energy absorption, and energy dissipation among the foam, gyroid lattices, and IPC structures.

DIC analysis was performed using the open-source MATLAB-based software Ncorr (v1.2.2) [56], which employs a region-growing DIC (RG-DIC) framework combined with an inverse compositional Gauss–Newton iterative solver for robust full-field displacement tracking. For the large-deformation compression of IPCs, high-strain analysis was enabled using seed propagation with automatic propagation to incrementally update the reference image and maintain correlation robustness under severe deformation. We ensured that the sample's imaging surfaces were uniformly speckled with consistent speckle size distribution. A subset-based correlation approach was employed, where the subset radius and strain radius were selected as the smallest values that minimizes noise while preserving spatial resolution. We computed the displacement gradients using a least-squares plane fit over a local circular neighborhood. We then calculated the Euler–Almansi finite strain tensors from the displacement gradients in the current configuration, enabling accurate characterization of the large compressive strains and localized deformation fields that evolved during IPC densification [57].

Acknowledgement

We acknowledge the partial support from the U. S. Office of Naval Research under PANTHER award number N00014-21-1-2916 and N00014-24-1-2200 through Dr. Timothy Bentley. We also acknowledge the partial support from the University of Wisconsin-Madison MRSEC (NSF-DMR-172041). JC and ED acknowledge the partial support from National Science Foundation (No. 2502930). Any opinion, findings, and conclusions or recommendations expressed in this material are those of the authors(s) and do not necessarily reflect the views of the National Science Foundation. We also acknowledge access to the Phenom Desktop SEM and the CT scan facility at the Core Laboratory for In-situ Facilities and Frontier Instruments (CLiFF) at CePaST, Florida A&M University, which was financially supported by the National Science Foundation (MRI-1726035), the Department of Defense (W911NF2210148), and FAMU Vice President of Research. The lab is powered by the management of the Dept. of Education RDI-ASPIRE program (P116H230039). The resources provided by this user facility were instrumental in conducting advanced characterization and analysis for this study.

Reference

[1] Baumeister J, Banhart J, Weber M. Aluminium foams for transport industry. Mater Des 1997;18:217–20. https://doi.org/10.1016/S0261-3069(97)00050-2.

[2] Lee ST. Introduction: Polymeric Foams, Mechanisms, and Materials. Polym. Foams, CRC Press; 2004.

[3] Ashby MF. The properties of foams and lattices. Philos Trans R Soc Math Phys Eng Sci 2005;364:15–30. https://doi.org/10.1098/rsta.2005.1678.

[4] Lefebvre L-P, Banhart J, Dunand DC. Porous Metals and Metallic Foams: Current Status and Recent Developments. Adv Eng Mater 2008;10:775–87. https://doi.org/10.1002/adem.200800241.
[5] Kulkarni SG, Gao X-L, Horner SE, Zheng JQ, David NV. Ballistic helmets – Their design, materials, and performance against traumatic brain injury. Compos Struct 2013;101:313–31. https://doi.org/10.1016/j.compstruct.2013.02.014.
[6] Rahimidehgolan F, Altenhof W. Compressive behavior and deformation mechanisms of rigid polymeric foams: A review. Compos Part B Eng 2023;253:110513. https://doi.org/10.1016/j.compositesb.2023.110513.
[7] Tomin M, Kmetty Á. Polymer foams as advanced energy absorbing materials for sports applications—A review. J Appl Polym Sci 2022;139:51714. https://doi.org/10.1002/app.51714.
[8] Kim JH, Kim D, Lee M-G, Lee JK. Multiscale Analysis of Open-Cell Aluminum Foam for Impact Energy Absorption. J Mater Eng Perform 2016;25:3977–84. https://doi.org/10.1007/s11665-016-2187-0.
[9] Pham TM, Chen W, Kingston J, Hao H. Impact response and energy absorption of single phase syntactic foam. Compos Part B Eng 2018;150:226–33. https://doi.org/10.1016/j.compositesb.2018.05.057.
[10] Yang X, Xia Y, Zhou Q. Influence of stress softening on energy-absorption capability of polymeric foams. Mater Des 2011;32:1167–76. https://doi.org/10.1016/j.matdes.2010.10.024.
[11] Avalle M, Belingardi G, Montanini R. Characterization of polymeric structural foams under compressive impact loading by means of energy-absorption diagram. Int J Impact Eng 2001;25:455–72. https://doi.org/10.1016/S0734-743X(00)00060-9.
[12] Menges G, Knipschild F. Estimation of mechanical properties for rigid polyurethane foams. Polym Eng Sci 1975;15:623–7. https://doi.org/10.1002/pen.760150810.
[13] Chen C, Airoldi A, Caporale AM, Sala G, Yin X. Impact response of composite energy absorbers based on foam-filled metallic and polymeric auxetic frames. Compos Struct 2024;331:117916. https://doi.org/10.1016/j.compstruct.2024.117916.
[14] Kucukkalfa E, Ok O, Yildiz K. Energy Absorption Characteristics of Elastomeric Nanoparticle Reinforced Polymeric Foam-Filled Auxetic Structures Under Cyclic Compression. AIAA SCITECH 2024 Forum, American Institute of Aeronautics and Astronautics; 2024. https://doi.org/10.2514/6.2024-1220.
[15] Zhang Z, Huang L, Li B, Chen T, Zhang Q, Jin F. Design of a novel multi-walled tube-reinforced aluminum foam for energy absorption. Compos Struct 2021;276:114584. https://doi.org/10.1016/j.compstruct.2021.114584.
[16] Lu W, Qin F, Zhang Q, Remillat C, Wang H, Scarpa F, et al. Engineering foam skeletons with multilayered graphene oxide coatings for enhanced energy dissipation. Compos Part Appl Sci Manuf 2020;137:106035. https://doi.org/10.1016/j.compositesa.2020.106035.
[17] Karsandik Y, Sabuncuoglu B, Yildirim B, Silberschmidt VV. Impact behavior of sandwich composites for aviation applications: A review. Compos Struct 2023;314:116941. https://doi.org/10.1016/j.compstruct.2023.116941.
[18] Sebaey TA, Kumar Rajak D, Mehboob H. Internally stiffened foam-filled carbon fiber reinforced composite tubes under impact loading for energy absorption applications. Compos Struct 2021;255:112910. https://doi.org/10.1016/j.compstruct.2020.112910.
[19] Xiong J, Du Y, Mousanezhad D, Eydani Asl M, Norato J, Vaziri A. Sandwich Structures with Prismatic and Foam Cores: A Review. Adv Eng Mater 2019;21:1800036. https://doi.org/10.1002/adem.201800036.
[20] Huang S-Y, Lou C-W, Yan R, Lin Q, Li T-T, Chen Y-S, et al. Investigation on structure and impact-resistance property of polyurethane foam filled three-dimensional fabric reinforced sandwich flexible composites. Compos Part B Eng 2017;131:43–9. https://doi.org/10.1016/j.compositesb.2017.07.061.

[21] Naguib HE, Park CB, Reichelt N. Fundamental foaming mechanisms governing the volume expansion of extruded polypropylene foams. J Appl Polym Sci 2004;91:2661–8. https://doi.org/10.1002/app.13448.
[22] Wu G, Xie P, Yang H, Dang K, Xu Y, Sain M, et al. A review of thermoplastic polymer foams for functional applications. J Mater Sci 2021;56:11579–604. https://doi.org/10.1007/s10853-021-06034-6.
[23] Wang X, Jiang M, Zhou Z, Gou J, Hui D. 3D printing of polymer matrix composites: A review and prospective. Compos Part B Eng 2017;110:442–58. https://doi.org/10.1016/j.compositesb.2016.11.034.
[24] Wang Z, Luan C, Liao G, Yao X, Fu J. Mechanical and self-monitoring behaviors of 3D printing smart continuous carbon fiber-thermoplastic lattice truss sandwich structure. Compos Part B Eng 2019;176:107215. https://doi.org/10.1016/j.compositesb.2019.107215.
[25] Benedetti M, du Plessis A, Ritchie RO, Dallago M, Razavi N, Berto F. Architected cellular materials: A review on their mechanical properties towards fatigue-tolerant design and fabrication. Mater Sci Eng R Rep 2021;144:100606. https://doi.org/https://doi.org/10.1016/j.mser.2021.100606.
[26] Jiang H, Bednarcyk BA, Le Barbenchon L, Chen Y. Elastically anisotropic architected metamaterials with enhanced energy absorption. Thin-Walled Struct 2023;192:111115. https://doi.org/10.1016/j.tws.2023.111115.
[27] Ferdousi S, Advincula R, Sokolov AP, Choi W, Jiang Y. Investigation of 3D printed lightweight hybrid composites via theoretical modeling and machine learning. Compos Part B Eng 2023;265:110958. https://doi.org/10.1016/j.compositesb.2023.110958.
[28] Cai J, Chin KCH, Gupta A, Boydston AJ, Thevamaran R. Overcoming Dynamic Stiffness-Damping Trade-Off with Structural Gradients in 3D Printed Elastomeric Gyroid Lattices. Exp Mech 2025;65:821–34. https://doi.org/10.1007/s11340-025-01165-2.
[29] Osman MM, Shazly M, El-Danaf EA, Jamshidi P, Attallah MM. Compressive behavior of stretched and composite microlattice metamaterial for energy absorption applications. Compos Part B Eng 2020;184:107715. https://doi.org/10.1016/j.compositesb.2019.107715.
[30] Zhang Z, Wang K, Bednarcyk BA, Le Barbenchon L, Chen Y. Tailoring the architecture of fractal lattice metamaterials for tunable energy absorption. Compos Part B Eng 2025;305:112711. https://doi.org/10.1016/j.compositesb.2025.112711.
[31] Zhou S, Zhao Y, Zhang K, Xun Y, Tao X, Yan W, et al. Impact-resistant supercapacitor by hydrogel-infused lattice. Nat Commun 2024;15:6481. https://doi.org/10.1038/s41467-024-50707-0.
[32] Dong L, Deshpande V, Wadley H. Mechanical response of Ti–6Al–4V octet-truss lattice structures. Int J Solids Struct 2015;60–61:107–24. https://doi.org/10.1016/j.ijsolstr.2015.02.020.
[33] Song J, Zhou W, Wang Y, Fan R, Wang Y, Chen J, et al. Octet-truss cellular materials for improved mechanical properties and specific energy absorption. Mater Des 2019;173:107773. https://doi.org/10.1016/j.matdes.2019.107773.
[34] Ajdari A, Jahromi BH, Papadopoulos J, Nayeb-Hashemi H, Vaziri A. Hierarchical honeycombs with tailorable properties. Int J Solids Struct 2012;49:1413–9. https://doi.org/10.1016/j.ijsolstr.2012.02.029.
[35] Cheng Y, Li J, Qian X, Rudykh S. 3D printed recoverable honeycomb composites reinforced by continuous carbon fibers. Compos Struct 2021;268:113974. https://doi.org/10.1016/j.compstruct.2021.113974.
[36] Abueidda DW, Elhebeary M, Shiang C-S (Andrew), Pang S, Abu Al-Rub RK, Jasiuk IM. Mechanical properties of 3D printed polymeric Gyroid cellular structures: Experimental and finite element study. Mater Des 2019;165:107597. https://doi.org/10.1016/j.matdes.2019.107597.
[37] Junaedi H, Abd El-baky MA, Awd Allah MM, Sebaey TA. Mechanical Characteristics of Sandwich Structures with 3D-Printed Bio-Inspired Gyroid Structure Core and Carbon Fiber-Reinforced Polymer Laminate Face-Sheet. Polymers 2024;16:1698. https://doi.org/10.3390/polym16121698.
[38] Ullah I, Brandt M, Feih S. Failure and energy absorption characteristics of advanced 3D truss core structures. Mater Des 2016;92:937–48. https://doi.org/10.1016/j.matdes.2015.12.058.

[39] Pham M-S, Liu C, Todd I, Lertthanasarn J. Damage-tolerant architected materials inspired by crystal microstructure. Nature 2019;565:305–11. https://doi.org/10.1038/s41586-018-0850-3.
[40] Qi D, Hu W, Xin K, Zeng Q, Xi L, Tao R, et al. In-situ synchrotron X-ray tomography investigation of micro lattice manufactured with the projection micro-stereolithography (PμSL) 3D printing technique: Defects characterization and in-situ shear test. Compos Struct 2020;252:112710. https://doi.org/10.1016/j.compstruct.2020.112710.
[41] Ma K, Gupta A, Srivastava V, Guduru P, Bazilevs Y. Polymer-based architected materials and structures: Geometry, experiments, constitutive modeling, and advanced simulations. Int J Solids Struct 2026;331:113911. https://doi.org/10.1016/j.ijsolstr.2026.113911.
[42] Li X, Tan YH, Wang P, Su X, Willy HJ, Herng TS, et al. Metallic microlattice and epoxy interpenetrating phase composites: Experimental and simulation studies on superior mechanical properties and their mechanisms. Compos Part Appl Sci Manuf 2020;135:105934. https://doi.org/10.1016/j.compositesa.2020.105934.
[43] Asar A, Zaki W. A comprehensive review of the mechanisms and structure of interpenetrating phase composites with emphasis on metal-metal and polymer-metal variants. Compos Part B Eng 2024;275:111314. https://doi.org/10.1016/j.compositesb.2024.111314.
[44] Prajapati MJ, Kumar A, Lin S-C, Jeng J-Y. Multi-material additive manufacturing with lightweight closed-cell foam-filled lattice structures for enhanced mechanical and functional properties. Addit Manuf 2022;54:102766. https://doi.org/10.1016/j.addma.2022.102766.
[45] Chapkin WA, Simone DL, Frank GJ, Baur JW. Mechanical behavior and energy dissipation of infilled, composite Ti-6Al-4V trusses. Mater Des 2021;203:109602. https://doi.org/10.1016/j.matdes.2021.109602.
[46] Kim K, Kim G, Kim HG, Kim HJ, Kim N. Customizing the mechanical properties of additively manufactured metallic meta grain structure with sheet-based gyroid architecture. Sci Rep 2022;12:19897. https://doi.org/10.1038/s41598-022-24207-4.
[47] Scherer MRJ. Double-Gyroid-Structured Functional Materials. Springer Science & Business Media; 2013.
[48] Li D, Liao W, Dai N, Dong G, Tang Y, Xie YM. Optimal design and modeling of gyroid-based functionally graded cellular structures for additive manufacturing. Comput-Aided Des 2018;104:87–99. https://doi.org/10.1016/j.cad.2018.06.003.
[49] Gibson LJ, Ashby MF. Cellular solids : structure and properties. Cambridge ; New York : Cambridge University Press; 1997.
[50] Liu H, Abdolrahim N. A modified scaling law for stiffness of nanoporous materials based on gyroid cell model. Int J Mech Sci 2020;166:105223. https://doi.org/10.1016/j.ijmecsci.2019.105223.
[51] Khaderi SN, Deshpande VS, Fleck NA. The stiffness and strength of the gyroid lattice. Int J Solids Struct 2014;51:3866–77. https://doi.org/10.1016/j.ijsolstr.2014.06.024.
[52] Choudhry NK, Panda B, Kumar S. Enhanced energy absorption performance of 3D printed 2D auxetic lattices. Thin-Walled Struct 2023;186:110650. https://doi.org/10.1016/j.tws.2023.110650.
[53] Ren H, Shen H, Ning J. Effect of Internal Microstructure Distribution on Quasi-Static Compression Behavior and Energy Absorption of Hollow Truss Structures. Materials 2020;13:5094. https://doi.org/10.3390/ma13225094.
[54] Baumeister J, Banhart J, Weber M. Aluminium foams for transport industry. Mater Des 1997;18:217–20. https://doi.org/10.1016/S0261-3069(97)00050-2.
[55] Gupta A, Chawla K, Maheswaran B, Syrlybayev D, Thevamaran R. Embracing nonlinearity and geometry: a dimensional analysis guided design of shock absorbing materials. Nat Commun 2025;16:7148. https://doi.org/10.1038/s41467-025-60300-8.
[56] Greenwald RM, Gwin JT, Chu JJ, Crisco JJ. Head impact severity measures for evaluating mild traumatic brain injury risk exposure. Neurosurgery 2008;62:789. https://doi.org/10.1227/01.neu.0000318162.67472.ad.
[57] Siegkas P, Sharp DJ, Ghajari M. The traumatic brain injury mitigation effects of a new viscoelastic add-on liner. Sci Rep 2019;9:3471. https://doi.org/10.1038/s41598-019-39953-1.

[58] Blaber J, Adair B, Antoniou A. Ncorr: Open-Source 2D Digital Image Correlation Matlab Software. Exp Mech 2015;55:1105–22. https://doi.org/10.1007/s11340-015-0009-1.
[59] Van Mieghem B, Ivens J, Van Bael A. Consistency of Strain Fields and Thickness Distributions in Thermoforming Experiments Through Stereo DIC. Exp Tech 2016;40:1409–20. https://doi.org/10.1007/s40799-016-0143-4.